Introduction

This supplementary material provides additional details on the thermal properties selected for the lithospheric layers (Text S1). Moreover, the sensitivity analysis to the thermal properties is presented in Text S2, Figure S1 and Tables S1 and S2. The geothermal gradient every 3 km is shown in Figure S2. Figure S3 depicts the sediment thickness in the study area used in the thermal model from the CRUST1.0 dataset (Laske et al., 2013). A brief explanation on the selected earthquake magnitude types is provided in Text S4. Figure S4 shows the evolution of magnitude values versus time in the earthquake catalogue. Figure S5 displays the calculation of the magnitude of completeness of the catalogue in the two periods considered. The spatial variations for the magnitude of completeness are analyzed in Text S5. Text S6 reports the magnitude formulae used to calculate the moment magnitude from other magnitude scales. Figure S6 shows the histogram of standard deviations of the D10 and D90 depths, as obtained from bootstrapping of the selected earthquake catalog (see Section 3.2 in the main text for more information). Figure S7 contains the synthesis of the modelled hypocentral temperatures of the selected earthquake subset, including the reported errors in the hypocentral depths (panel d). Figure S8 shows the errors of the Moho depths reported in the GEMMA dataset (Reguzzoni & Sampietro, 2015). Lastly, Table S3 relates the mantle composition used in the conversion of S-wave velocities into mantle temperatures.

Text S1. Thermal properties assigned to the lithospheric layers

Most thermal conductivities were defined averaging the values reported by Turcotte & Schubert (2002) for particular lithologies. For example, the thermal conductivity for oceanic sediments was obtained by averaging the values of shale, sandstone and limestone. When direct rock samples were available, their composition was taken into account for selecting thermal conductivities, for example in the Aves Ridge.

The radiogenic heat production was mainly assigned considering the values reported by Vilà et al. (2010) for each lithology. In some cases, where specific sample analyses were available in the studied area, it was calculated using the actual concentration of the radioactive elements U, Th, and K (Eq. S1). This was the case for rocks of the Caribbean Large Igneous Plateau fragments reported by Kerr (2014), and for a few samples of the Aves Ridge, studied by Neill et al. (2011). The radiogenic heat production of the slab and lithospheric mantle were defined based on the average concentration of mantle rocks reported by Turcotte & Schubert (2002). In those cases, the equation that relates the radiogenic heat production (mW m^{-3}) with the radioactive composition is (Vilà et al., 2010):

$$RHP = 10^{-5}\rho(9.52C_U + 2.56C_{Th} + 3.48C_K) \qquad \text{Eq. S1}$$

Where ρ is the density (kg m^{-3}) obtained from the forward modelling of the gravity anomalies for each layer (Table 1, after Gómez-García et al., 2020, 2021), and C_U, C_{Th}, and C_K the concentration of uranium (ppm), thorium (ppm), and potassium (%), respectively.

A sensitivity test (Test S2) was performed to different thermal properties, and 25 models were implemented, aiming to explore the broad range of feasible thermal configurations given the lithologies of the study area. The best-fitting model was selected contrasting the resulting thermal field against available observations (borehole temperature and surface heat flow -Figure 3), and corresponds to the parameters presented in Table 1.

Text S2. Sensitivity analysis of thermal properties

We explored the sensitivity of the thermal field in the study area using 25 different thermal configurations. Although the thermal parameters of several layers were considered in these sensitivity tests, particular attention was given to the radiogenic heat production (Table S1) and thermal conductivity (Table S2) of the continental sediments, the continental upper and lower crusts, the slabs and lithospheric mantle, given the application of the model to crustal seismicity.

Figure S1 shows the statistics of the residual borehole temperature (observed minus modelled) for each model. The specific thermal configuration of each experiment is presented in Tables S1 and S2. We selected model 24 (M24) as the final one, because the mean value of the residuals is close to zero (4.99°C) and it has the minimum standard deviation (9.21°C).

This test demonstrates that the model is highly sensitive to the thermal properties assigned to the lithospheric layers; and therefore, fitting the observed temperature can be considered an adequate way of validating the resulting 3D thermal field. This also highlights the importance of having more temperature observations available in the future, as they could provide more control points for constraining the models.
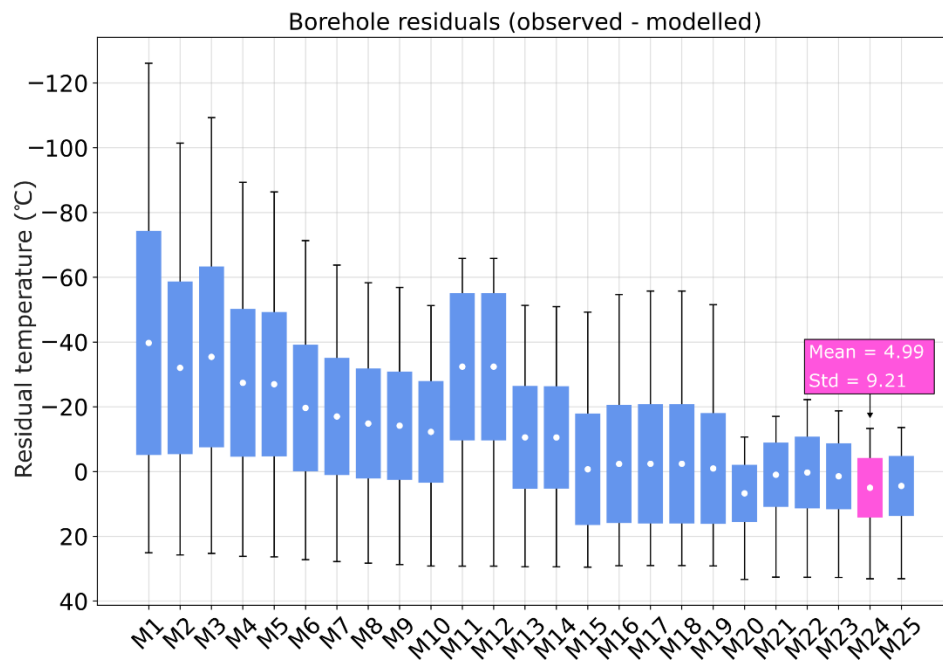
Figure S1. Borehole residual temperature associated to the 25 tested thermal models (details in Tables S1 and S2). The white dots correspond to the mean value of the residuals, the bars are the standard deviation and the black lines represent the range of the residuals. The location of the boreholes is presented in Figure 3.

Table S1. Values of radiogenic heat production assumed for the different layers of the tested models.

Radiogenic heat production (W m⁻³)																									
Layer	M1	M2	M3	M4	M5	M6	M7	M8	M9	M10	M11	M12	M13	M14	M15	M16	M17	M18	M19	M20	M21	M22	M23	M24	M25
Oceanic sediments	1.1																								
Continental sediments	1.19																								1.6
Oceanic upper crust	0.358																								
Low density bodies (Aves Ridge)	1.07																								
High density bodies in the upper oceanic crust	0.057																								
Oceanic lower crust	0.468																								
Low density bodies in the lower oceanic crust (Aves Ridge)	1.07																								
High density bodies in the lower oceanic crust	0.057																								
Continental upper crust	3.233	1.741	0.903																	0.6			0.9	0.6	

Radiogenic heat production (W m^{-3})																									
Layer	M1	M2	M3	M4	M5	M6	M7	M8	M9	M10	M11	M12	M13	M14	M15	M16	M17	M18	M19	M20	M21	M22	M23	M24	M25
Low density bodies in the upper continental crust	0.85									0.7								0.4							
High density body in the upper continental crust (Santa Marta massif)	0.677																								
Continental lower crust	0.85						0.7	0.5																	
High density subcrustal bodies	0.01																								
Slab	0.03		0.258	0.001																					
Lithospheric mantle	0.03			0.012																					

Table S2. Values of thermal conductivity assumed for the different layers of the tested models.

Layer	Thermal conductivity (W m⁻¹ K⁻¹)																								
	M1	M2	M3	M4	M5	M6	M7	M8	M9	M10	M11	M12	M13	M14	M15	M16	M17	M18	M19	M20	M21	M22	M23	M24	M25
Oceanic sediments	1.49																			2.55	2.3	2.55			
Continental sediments	2.55										1.5		2.55		3.5						3	3.5			
Oceanic upper crust	2.1																								
Low density bodies (Aves Ridge)	2.6																								
High density bodies in the upper oceanic crust	2.93																								
Oceanic lower crust	2.95																								
Low density bodies in the lower oceanic crust (Aves Ridge)	2.6																								
High density bodies in the lower oceanic crust	2.93																								

Thermal conductivity (W m^{-1} K^{-1})																									
Layer	M1	M2	M3	M4	M5	M6	M7	M8	M9	M10	M11	M12	M13	M14	M15	M16	M17	M18	M19	M20	M21	M22	M23	M24	M25
Continental upper crust	3.1				2.4				2.2					2.1			2.4								
Low density bodies in the upper continental crust	2.82										2.5	2.87	2.5	2.1											
High density body in the upper continental crust (Santa Marta massif)	2.95																								
Continental lower crust	2.82				2.4				1.9							2.4									
High density subcrustal bodies	4.15																								
Slab	4						3																4	3.3	
Lithospheric mantle	3.75						3.5		3																

(d) 9km - 12km

(e) 12km - 15km

(f) 15km - 18km
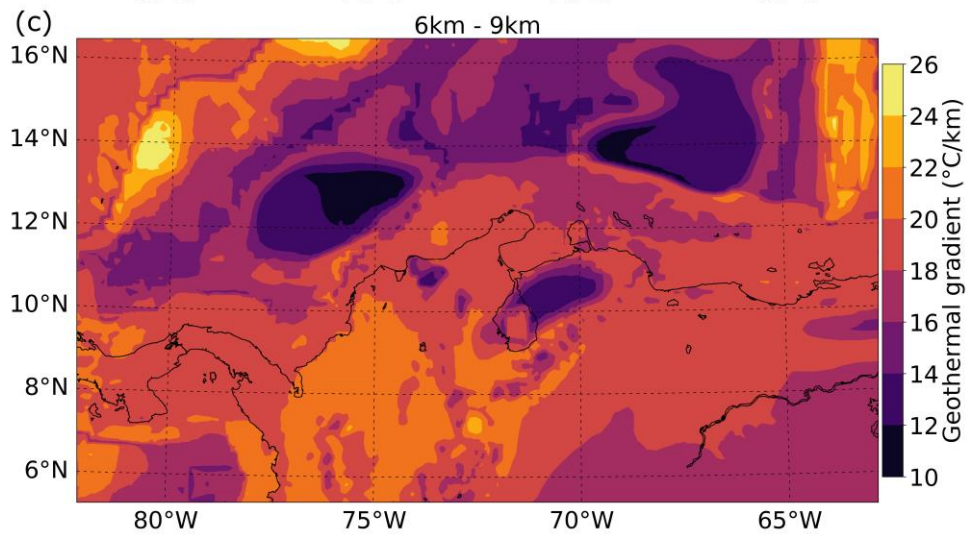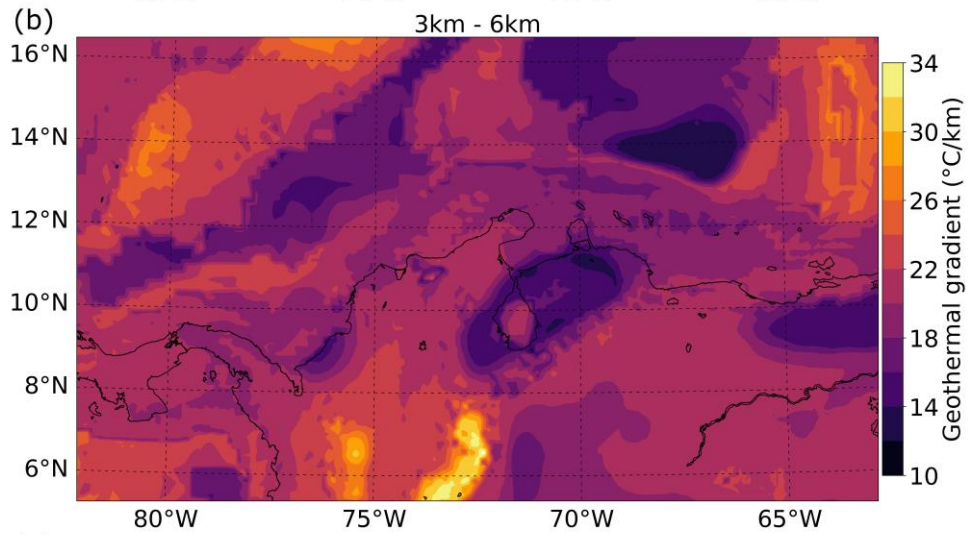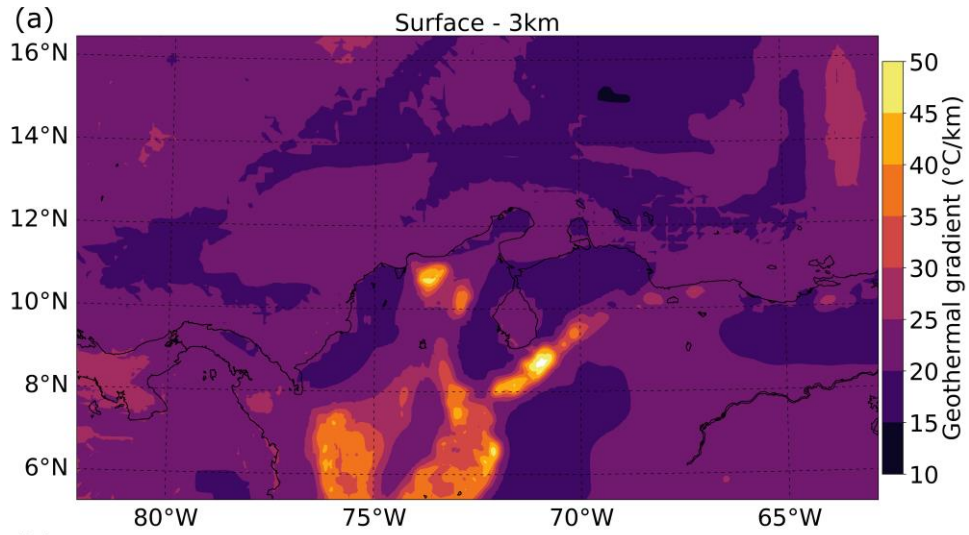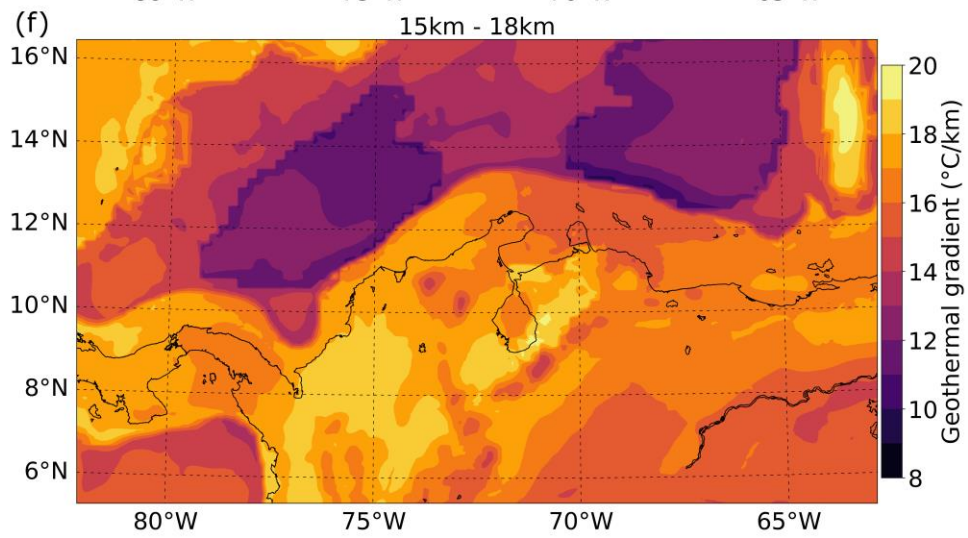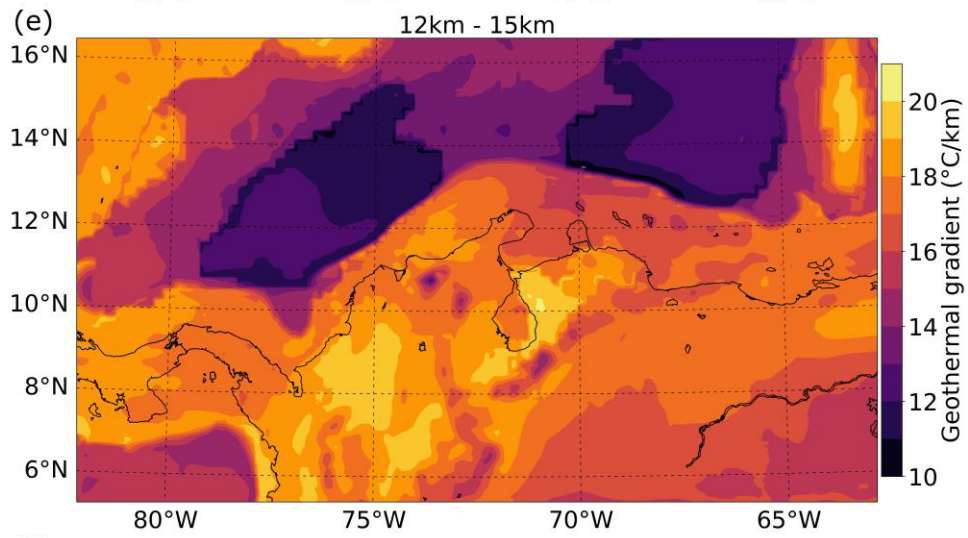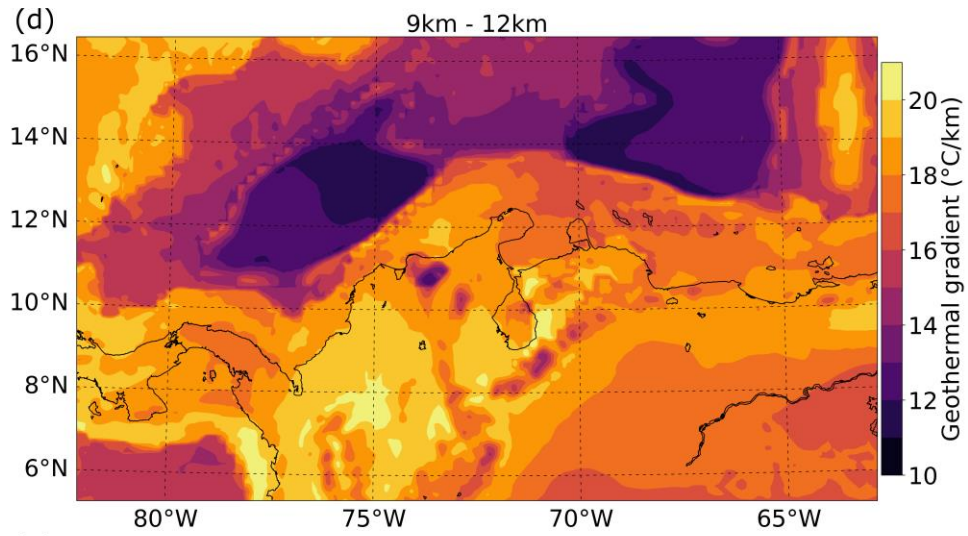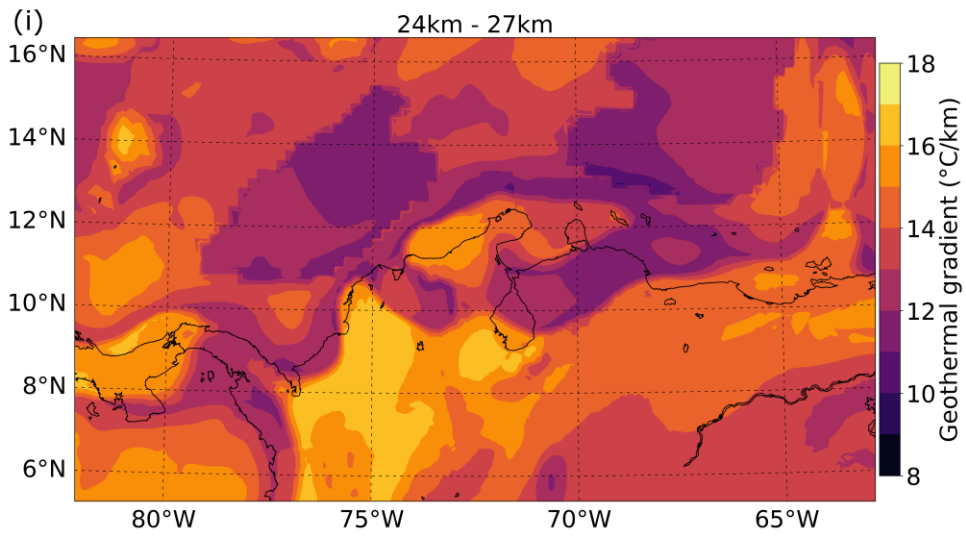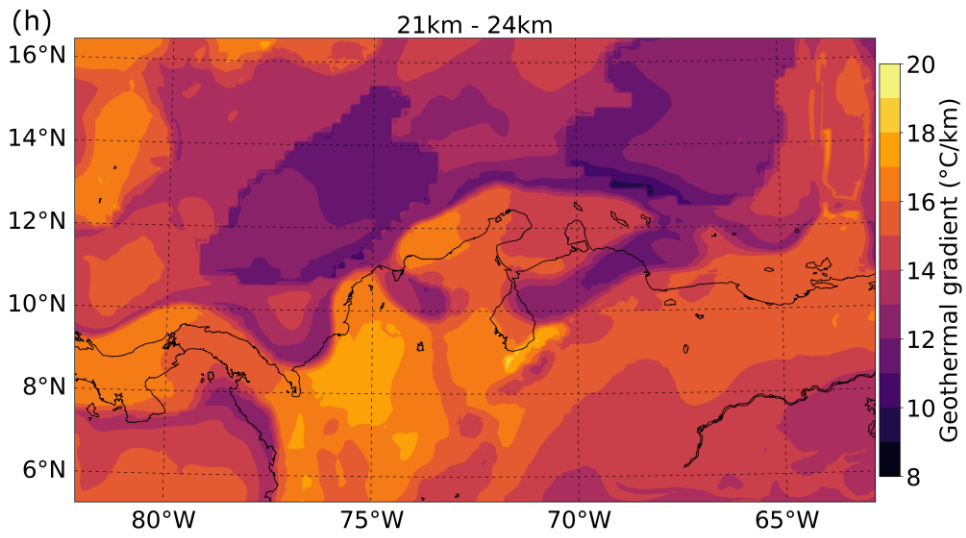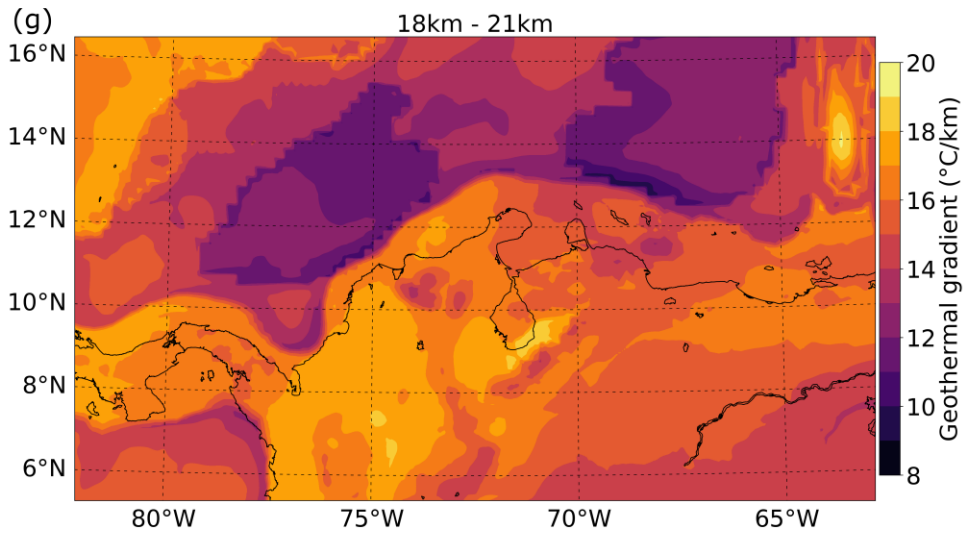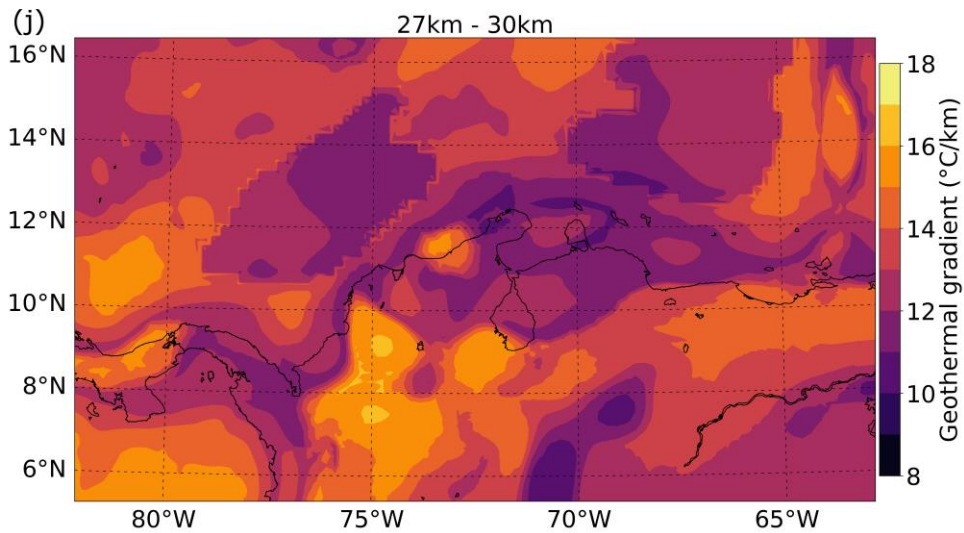
Figure S2. Geothermal gradient computed at different depth intervals based on the resulting thermal fields. (a) Surface down to 3 km depth. (b) 3 km to 6 km. (c) 6 km to 9 km. (d) 9 km to 12 km. (e) 12 km to 15 km. (f) 15 km to 18 km. (g) 18 km to 21 km. (h) 21 km to 24 km. (i) 24 km to 27 km. (j) 27 km to 30 km. The range of values in the color bars are not the same for all figures.
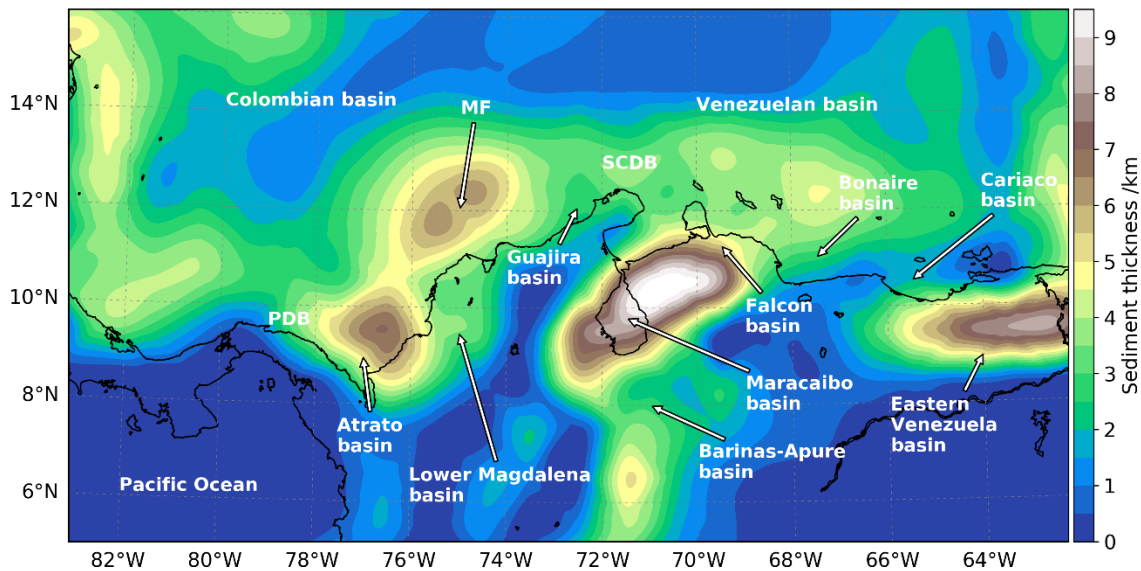
Figure S3. Sediment thickness in the study area (Laske et al., 2013) as parametrized in the thermal calculation. MF = Magdalena Fan. PDB = Panamá Deformed Belt. SCDB = South Caribbean Deformed Belt.

Text S4. Selection of earthquake magnitude types

We adopted the hierarchy proposed by ISC for selecting the most reliable, preferred magnitude (Di Giacomo & Storchak, 2016), considering the magnitude types reported in the study region. Namely, using the abbreviations from the original ISC Bulletin, the hierarchy is: 1) MW, Mw or Mwr (moment magnitude); 2) MS (teleseismic surface-wave magnitude) or MsBB (its equivalent from broad-band

records; Di Giacomo & Storchak, 2022); 3) mB (broadband body-wave magnitude; Bormann and Saul, 2008); 4) mb (teleseismic, short-period body-wave magnitude); 5) ML, MLv, or mL (local magnitude); 6) MD or md (duration magnitude) and 7) Any other local or regional magnitude. If there were several values for the preferred magnitude type, the largest one was chosen for simplicity. We disregarded events located in the region but without reported magnitude.
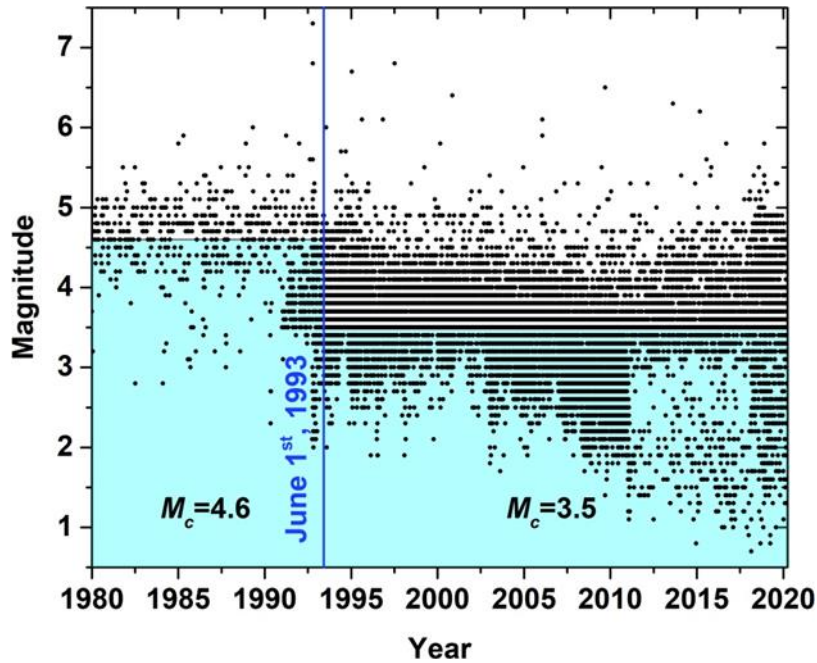
Figure S4. Preferred magnitude versus time of earthquakes with depth ≤ 50 km (including all crustal seismicity) in the whole study area (5° to 15°, 63° to 82° W), reported in the reviewed ISC Bulletin (International Seismological Centre, 2022). This kind of scatterplot is useful for identifying heterogeneities and different periods in the compilation of an earthquake catalog (e.g.: Gentili et al., 2011; González, 2017). Note that very few earthquakes with magnitude <4.0 were recorded before 1991, indicating incompleteness at least below this value for that period. Earthquakes with magnitudes <3.5 have been recorded only irregularly, and more frequently since June 1993, when the Colombian national seismic network started to compile its earthquake catalog (Arcila *et al.*, 2020) and reporting data to ISC. This date (vertical line) was chosen for separating the whole catalogue into two sub-periods, with different magnitude of completeness (M_c, see following figure).
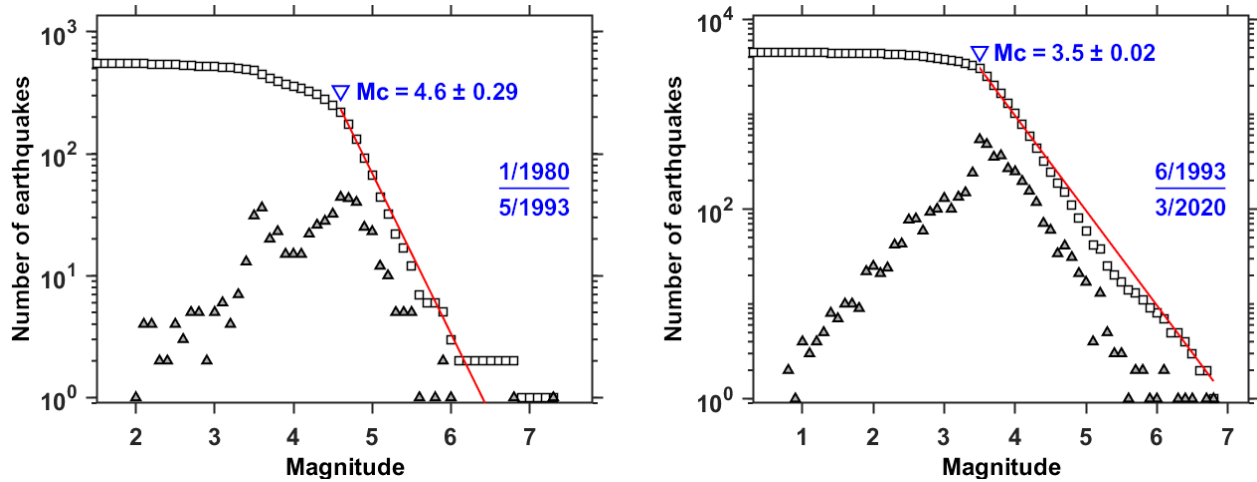
Figure S5. Magnitude of completeness of the earthquake catalogue, in the two sub-periods considered. *Triangles*: Number of earthquakes in each magnitude bin (0.1 units wide). *Squares*: Cumulative number of earthquakes with magnitude greater or equal than stated. *Mc*: Magnitude of completeness calculated with the maximum curvature method (Wiemer & Wyss, 1997), with uncertainty calculated using 1000 bootstrap samples (Woessener & Wiemer, 2005). This is the same method used by Woessener & Wiemer (2005) with the ISC Bulletin. *Red lines*: Maximum-likelihood Gutenberg-Richter fits to the cumulative distributions, for the complete part of each catalogue subset. The fits are not used for calculating M_c with this method, and are only shown as reference, to indicate that they hold for magnitude $\geq M_c$. Note the different scales in both plots. Calculations and plots were made with ZMAP v. 6.0 (Wiemer, 2001).

Text S5. Spatial variations of the magnitude of completeness

The calculated spatial variations of M_c in the region are smaller than the temporal ones. The number of earthquakes, particularly in the first period, was too low to calculate M_c with as much spatial detail as D10 or D90, given that M_c requires a very minimum of 60 events in the sample (e.g. Woessner & Wiemer, 2005, González, 2017), while D10 or D90 may start to be estimated with a third of that figure. An attempt was made of mapping M_c in detail in each period, with a fixed radius of 120 km around the nodes of a latitude/longitude grid in steps of 0.1 degrees latitude/longitude and the maximum curvature method, with uncertainties calculated with 200 bootstraps (Woessner & Wiemer, 2005). In the first period, no region had significantly higher M_c (where it could be calculated) than the mean. In the second period, M_c was significantly higher than the mean (M_c ~4) only south of Panama and at the volcanic San Andrés Archipelago, areas whose results are not interpreted in this work. So in all of the sub-regions analyzed in the main text, M_c was not significantly higher (worse) than the mean values used for the analysis.

Text S6. Formulae used for calculating moment magnitude from other magnitude scales

If the preferred magnitude from the ISC Bulletin was not already M_W, it was converted using these relations:

- From body-wave magnitude (m_b): $M_W = e^{(-4.664+0.859 \times m_b)} + 4.555$ (Di Giacomo *et al.*, 2015)
- From surface-wave magnitude (M_s): $M_W = e^{(-0.222+0.233 \times M_S)} + 2.863$ (Di Giacomo *et al.*, 2015)
- From local magnitude (M_L): $M_W = 0.958 \times M_L + 0.1$ (Arcila *et al.*, 2020)

- From duration magnitude (M_D): $M_W = 2.189 + 0.660 \times M_D$ (Salazar *et al.*, 2013).
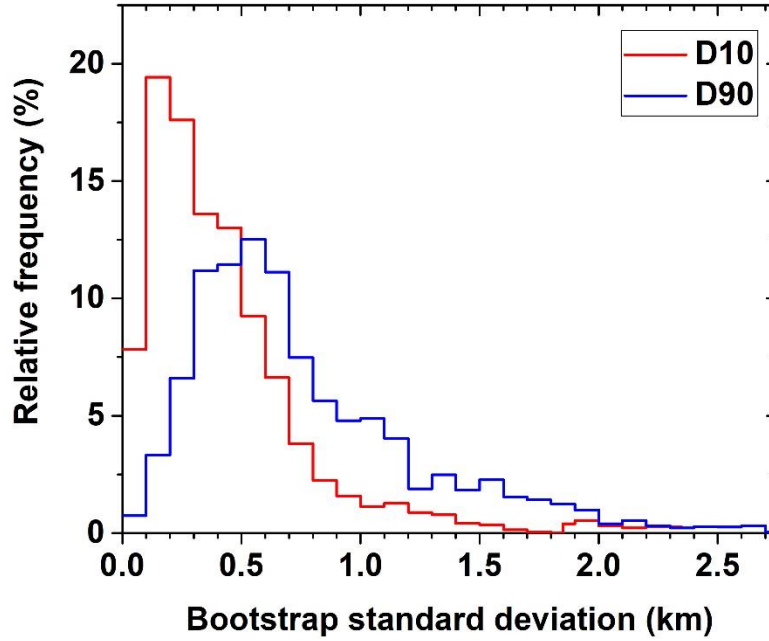
Figure S6. Histogram of standard deviations of D10 and D90 calculated from bootstrapping.
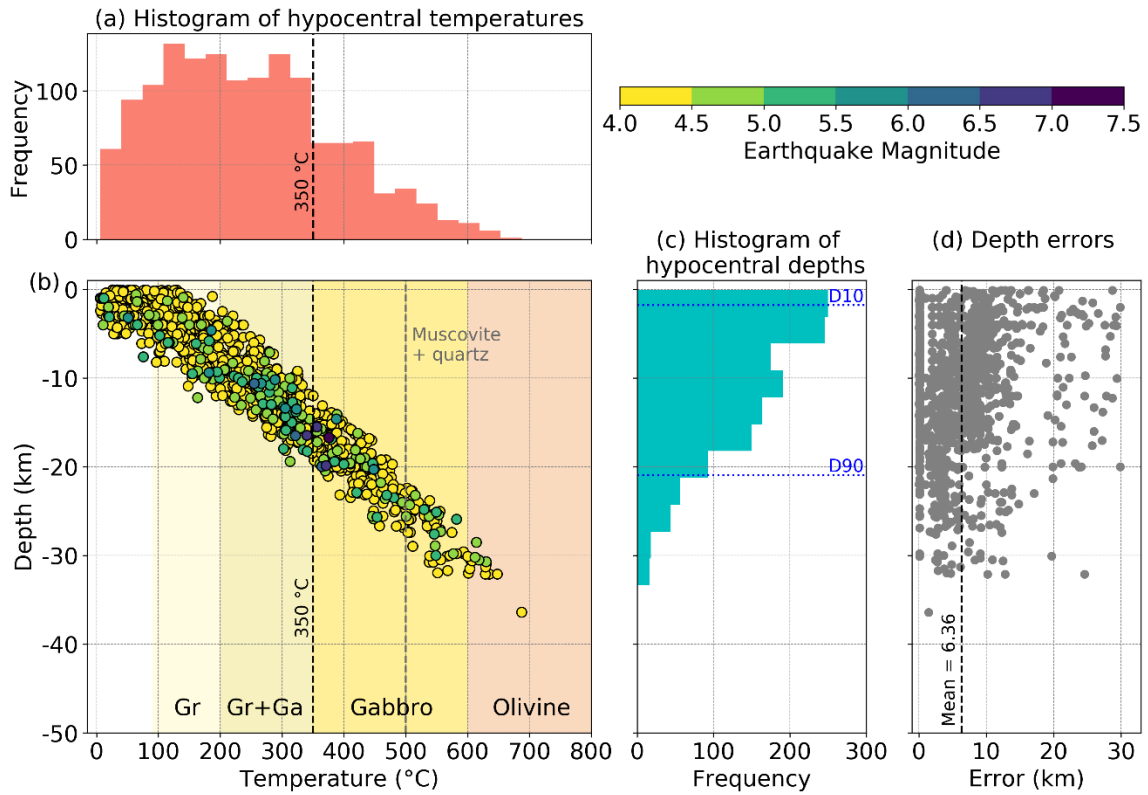
Figure S7. Synthesis of the modelled temperatures. (a) Histogram of hypocentral temperatures. (b) Modelled temperatures versus depth and preferred magnitude. Different colored domains represent the

seismogenic windows of different rocks/minerals. Gr = Granite. Gr+Ga = shared seismogenic window between granite and gabbro. (c) Histogram of hypocentral depths, with regional D10 = 1.8 km and D90 = 20.9 km. (d) Hypocentral errors associated to the selected earthquakes.
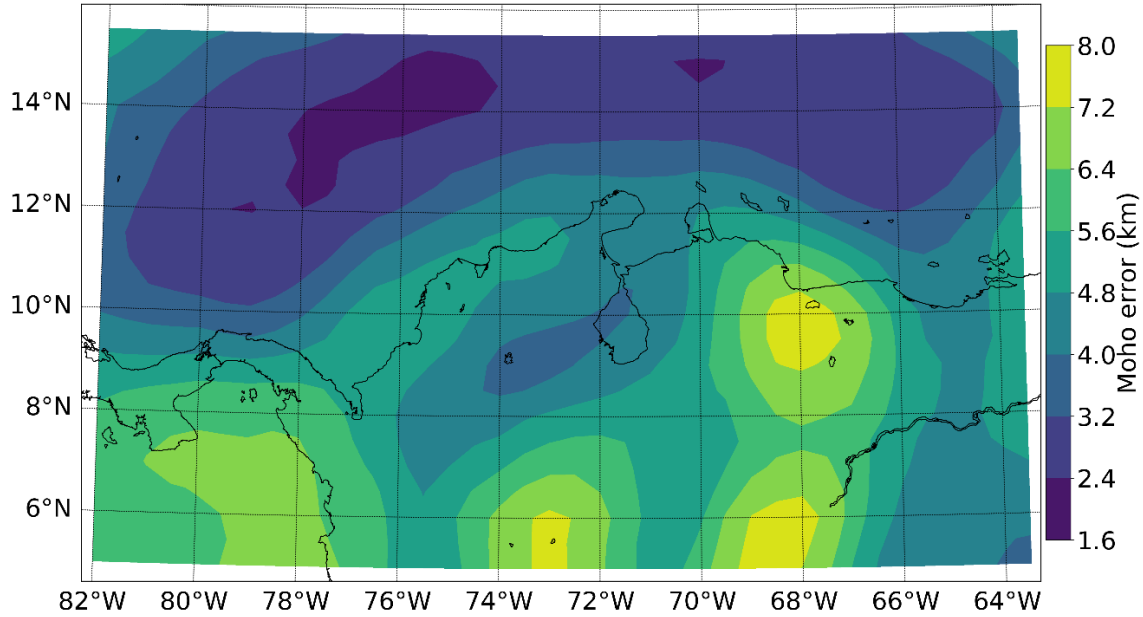
Figure S8. Errors associated to the Moho depths used in this study according to the GEMMA dataset (Reguzzoni & Sampietro, 2015), interpolated to a resolution of 0.5°.

Phase	Fraction
Olivine	0.75
Clinopyroxene	0.035
Orthopyroxene	0.21
Garnet	0
Jadeite	0.005
XFe	0.01

Table S3. Mantle composition (based on Shapiro & Ritzwoller, 2004) assumed in the conversion of S-wave velocities (Schaeffer & Lebedev, 2013) to temperatures at 75 km depth.

References

Arcila, M., García, J., Montejo, J., Eraso, J., Valcarcel, J., Mora, M., Viganò, D., Pagani, M., & Díaz, F. (2020). *Modelo nacional de amenaza sísmica para Colombia*. Ed.: Servicio Geológico Colombiano & Global Earthquake Model Foundation. Bogotá (Colombia). 308 p. http://doi.org/10.32685/9789585279469

Bormann, P., & Saul, J. (2008). The new IASPEI standard broadband magnitude mB. *Seismological Research Letters, 79*(5), 698–705. https://doi.org/10.1785/gssrl.79.5.698

Di Giacomo, D., Bondár, I., Storchak, D. A., Engdahl, E. R., Bormann, P., & Harris, J. (2015). ISC-GEM Global Instrumental Earthquake Catalogue (1900-2009), III. Re-computed M_s and m_b, proxy M_W, final magnitude composition and completeness assessment. *Physics of the Earth and Planetary Interiors*, *239*, 33–47. https://doi.org/10.1016/j.pepi.2014.06.005

Di Giacomo, D., & Storchak, D. A. (2016). A scheme to set preferred magnitudes in the ISC Bulletin. *Journal of Seismology*, *20*(2), 555–567. https://doi.org/10.1007/s10950-015-9543-7

Di Giacomo, D., & Storchak, D. A. (2022). One hundred plus years of recomputed surface wave magnitude of shallow global earthquakes. *Earth System Science Data*, *14*(2), 393–409. https://doi.org/10.5194/essd-14-393-2022

Gentili, S., Sugan, M., Peruzza, L. & Schorlemmer, D. (2011). Probabilistic completeness assessment of the past 30 years of seismic monitoring in northeastern Italy. *Physics of the Earth and Planetary Interiors*, 186(1–2), 81–96, doi:10.1016/j.pepi.2011.03.005.

Gómez-García, Á. M., Le Breton, E., Scheck-Wenderoth, M., Monsalve, G., & Anikiev, D. (2020). 3D lithospheric structure of the Caribbean and north South American Plates and Rotation Files of Kinematic Reconstructions back to 90 Ma of the Caribbean Large Igneous Plateau. *GFZ data services*, https://doi.org/https://doi.org/10.5880/GFZ.4.5.2020.003

Gómez-García, Á. M., Le Breton, E., Scheck-Wenderoth, M., Monsalve, G., & Anikiev, D. (2021). The preserved plume of the Caribbean Large Igneous Plateau revealed by 3D data-integrative models. *Solid Earth*, *12*(1), 275–298. https://doi.org/10.5194/se-12-275-2021

González, Á. (2017). The Spanish National Earthquake Catalogue: Evolution, precision and completeness. *Journal of Seismology*, 21(3), 435–471, doi:10.1007/s10950-016-9610-8

Kerr, A. C. (2014). Oceanic Plateaus. In *Treatise on Geochemistry: Second Edition* (2nd ed., Vol. 4, pp. 631–667). Oxford: Elsevier Ltd. https://doi.org/10.1016/B978-0-08-095975-7.00320-X

Laske, G., Masters, G., Ma, Z., & Pasyanos, M. E. (2013). CRUST1.0: An Updated Global Model of Earth's Crust. *Geophys. Res. Abstracts*, *15*, Abstract EGU2013--2658. Retrieved from http://igppweb.ucsd.edu/~gabi/rem.html

Neill, I., Kerr, A. C., Hastie, A. R., Stanek, K.-P., & Millar, I. L. (2011). Origin of the Aves Ridge and Dutch-Venezuelan Antilles: interaction of the Cretaceous "Great Arc" and Caribbean-Colombian Oceanic Plateau? *Journal of the Geological Society*, *168*(2), 333–348. https://doi.org/10.1144/0016-76492010-067

Reguzzoni, M., & Sampietro, D. (2015). GEMMA: An Earth crustal model based on GOCE satellite data. *International Journal of Applied Earth Observation and Geoinformation*, *35*(PA), 31–43. https://doi.org/10.1016/j.jag.2014.04.002

Salazar, W., Brown, L., Hernández, W., & Guerra, J. (2013). An earthquake catalogue for El Salvador and neighboring Central American countries (1528-2009) and its implication in the seismic hazard assessment. *Journal of Civil Engineering and Architecture*, *7*(8), 1018-1045. https://doi.org/10.17265/1934-7359/2013.08.011

Schaeffer, A. J., & Lebedev, S. (2013). Global shear speed structure of the upper mantle and transition zone. *Geophysical Journal International*, *194*(1), 417–449. https://doi.org/10.1093/gji/ggt095

Shapiro, N. M., & Ritzwoller, M. H. (2004). Thermodynamic constraints on seismic inversions. *Geophysical Journal International*, *157*(3), 1175–1188. https://doi.org/10.1111/j.1365-246X.2004.02254.x

Turcotte, D., & Schubert, G. (2002). *Geodynamics. Cambridge*.
https://doi.org/10.1017/CBO9781107415324.004

Vilà, M., Fernández, M., & Jiménez-Munt, I. (2010). Radiogenic heat production variability of some common lithological groups and its significance to lithospheric thermal modeling. *Tectonophysics*, *490*(3–4), 152–164. https://doi.org/10.1016/j.tecto.2010.05.003

Wiemer, S. (2001). A software package to analyze seismicity: ZMAP. *Seismological Research Letters*, 72, 373–382, https://doi.org/10.1785/gssrl.72.3.373

Wiemer, S. and Wyss, M. (1997). Minimum magnitude of completeness in earthquake catalogs: Examples from Alaska, the western United States, and Japan. *Bulletin of the Seismological Society of America*, 90, 859–869, https://doi.org/10.1785/0119990114

Woessner, J. & Wiemer, S. (2005): Assessing the quality of earthquake catalogues: Estimating the magnitude of completeness and its uncertainty. *Bulletin of the Seismological Society of America*, 95, 684–698, https://doi.org/10.1785/0120040007